

Extreme-ultraviolet wavelength and lifetime measurements in highly ionized krypton

K.W. Kukla, A.E. Livingston, C.M. Vogel Vogt, H.G. Berry, R.W. Dunford, L.J. Curtis, and S. Cheng

Abstract: We have studied the spectrum of highly ionized krypton in the extreme-ultraviolet wavelength region (50–300 Å), using beam-foil excitation of fast krypton ions at the Argonne ATLAS accelerator facility. We report measurements of transition wavelengths and excited-state lifetimes for $n = 2$ states in the lithiumlike, berylliumlike, and boronlike ions, $\text{Kr}^{31+,32+,33+}$. Excited state lifetimes ranging from 10 ps to 3 ns were measured by acquiring time-of-flight-delayed spectra with a position-sensitive multichannel detector.

PACS Nos.: 32.70.Cs, 32.30.Jc, 34.50.Fa

Résumé : Nous avons étudié le spectre du krypton hautement ionisé dans l'ultra-violet lointain (50–300 Å) par excitation faisceau-lame d'ions de krypton rapides produits par l'accélérateur ATLAS d'Argonne. Nous présentons des mesures de longueur d'onde de transition et de période radioactive pour les états excités $n = 2$ de $\text{Kr}^{31+,32+,33+}$, de types lithium, beryllium et bore. Les périodes radioactives d'états excités, entre 10 ps et 3 ns ont été mesurées par le spectre de temps de vol à délai obtenu à l'aide d'un détecteur multi-canaux à sensibilité spatiale.

[Traduit par la Rédaction]

1. Introduction

Few-electron ions are test beds for comparisons of accurate atomic structure calculations with precision experimental measurements. For ions as highly charged as lithiumlike, berylliumlike, and boronlike krypton, $\text{Kr}^{31+,32+,33+}$, relativity has a major influence on $2p_{3/2}$ electrons, much more so than on $2p_{1/2}$ electrons. This influence produces a significant shift in the spectral range of transitions to the $2s$ levels, as well as shortened level lifetimes. Kr is the heaviest element for which $2p_{3/2}$ level lifetimes have been measured so far. We report new measurements of transition wavelengths and excited state lifetimes for $n = 2$ states in $\text{Kr}^{31+,32+,33+}$ ions.

Received 6 September 2005. Accepted 4 November 2005. Published on the NRC Research Press Web site at <http://cjp.nrc.ca/> on 8 December 2005.

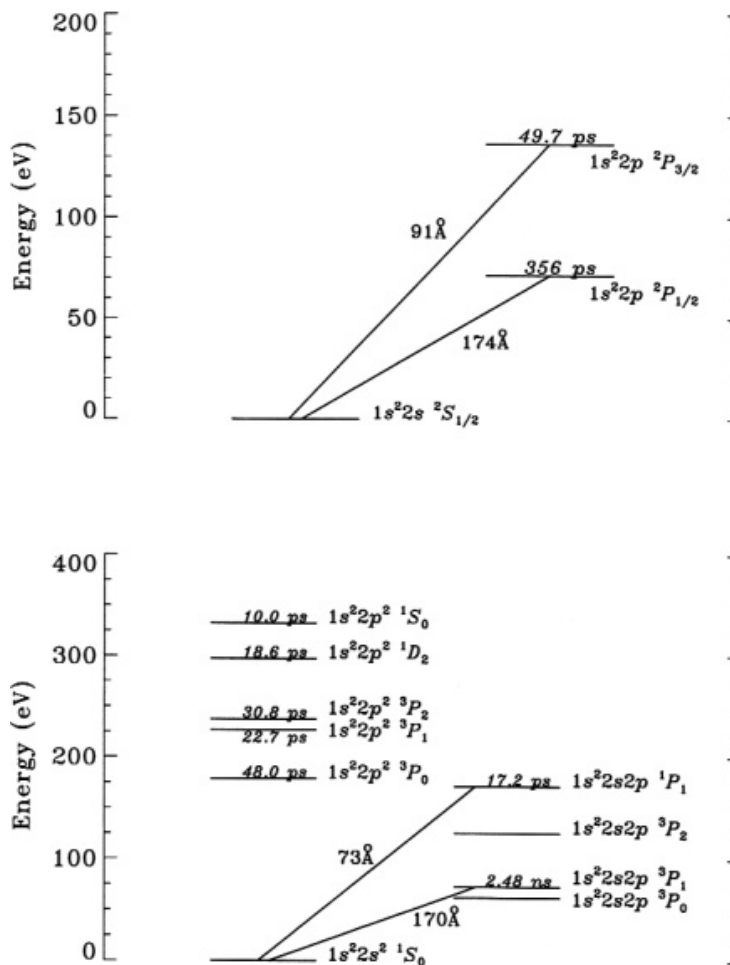
K.W. Kukla, A.E. Livingston, C.M. Vogel Vogt, and H.G. Berry. Department of Physics, University of Notre Dame, Notre Dame, IN 46556, USA.

R.W. Dunford. Chemistry Division, Argonne National Laboratory, Argonne, IL 60439, USA.

L.J. Curtis¹ and S. Cheng. Department of Physics, University of Toledo, Toledo, OH 43606, USA.

¹Corresponding author (e-mail: ljc@physics.utoledo.edu).

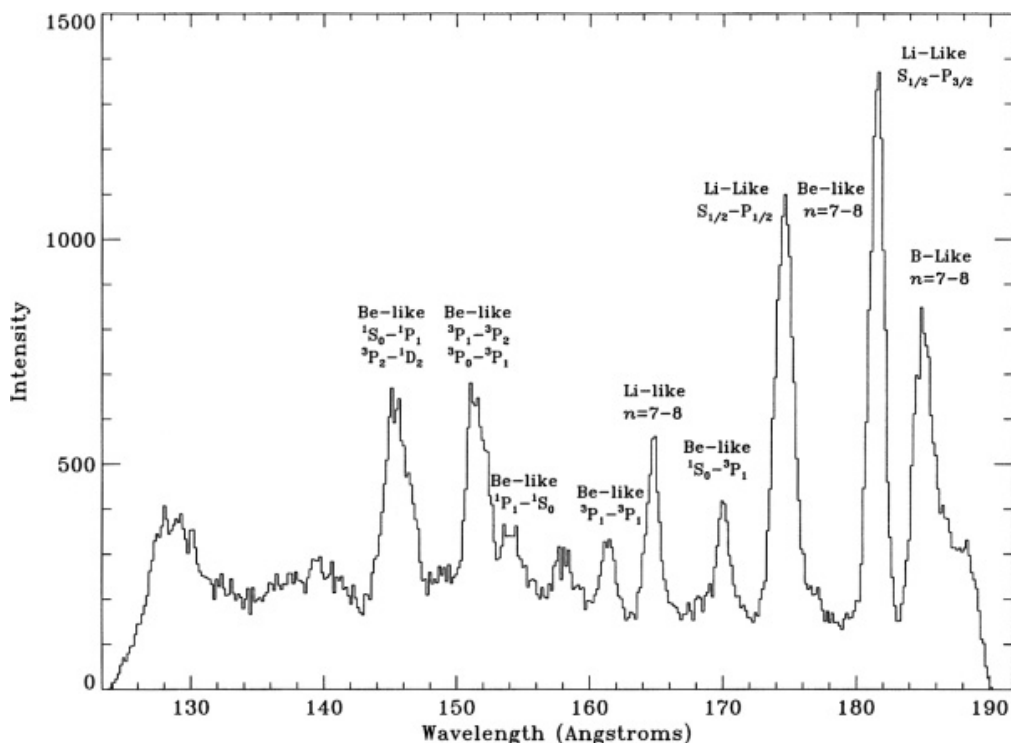
Fig. 1. Energy-level diagrams for the $n = 2$ states of lithiumlike and berylliumlike krypton ions.



2. Experiment

The emission spectrum of highly ionized krypton was produced using excitation of a fast beam of krypton ions by passage through a thin solid target. The electron cyclotron resonance ion source (ECRIS) injector at Argonne National Laboratory provided a beam of ^{84}Kr ions, which were accelerated in the ATLAS linear accelerator system. Separate experiments with krypton ions of final energies of 610 and 800 MeV were performed. The collimated ion beam was directed through a carbon target foil (thickness selected from 10 to $217 \mu\text{g}/\text{cm}^2$) and was stopped in a remote shielded Faraday cup. Typical beam currents on target ranged from 1 to 15 particle nA, depending on the ion energy and the incident (prestripped) charge state of the krypton ion beam.

The foil-excited fluorescence spectrum of highly ionized krypton was observed perpendicular to the beam direction using a 2.2 m, grazing incidence, vacuum ultraviolet (VUV) grating spectrometer (McPherson model 247). The spectrometer was set at an angle of incidence of 87.5° and employed an auxiliary entrance slit that shifted the effective angle of incidence to 86.6° . The entrance slit was displaced from its standard position to within millimetres of the ion beam, but still on the Rowland circle, to preserve focusing. Such a slit arrangement improves the spatial resolution at the ion beam [1, 2], a prerequisite for the measurement of atomic lifetimes of the order of ~ 10 ps. The entrance slit width used was typically $100 \mu\text{m}$.

Fig. 2. A highly ionized krypton spectrum recorded with a position sensitive detector.

Ultraviolet emission from the ion beam was dispersed using a 600 line/mm concave diffraction grating. VUV radiation was detected using a microchannel-plate (MCP) position-sensitive photoelectric detector (PSD) located in the exit plane of the spectrometer. The PSD provided for the simultaneous collection of spectroscopic data over a range of about 60 Å in first diffraction order. The multichannel observation not only enhanced the data collection efficiency, but also provided uniform sensitivity to time-dependent variations in the source or detector systems. The PSD assembly consisted of a pair of 25 mm diameter MCPs with a resistive anode position encoder, operated as a one-dimensional device. The angle between the detector normal and the optic axis was about 62°, optimizing the detection efficiency. The two position-sensing output voltage pulses from the anode were accumulated by computer in event mode to allow subsequent replay and analysis of data. A timing pulse was taken from the second MCP to enable signal gating. Using this timing pulse with the pulsed nature of the ATLAS beam provided the capability to eliminate a large fraction of the background signals [3].

3. Wavelengths

Prompt emission spectra (observation of the ion beam close to the foil) were measured over the wavelength region of 50–300 Å. The identified transitions belonged to the krypton ion charge states in the range predicted by equilibrium charge state distribution studies [4]. For the 610 MeV ion beam this meant transitions primarily from boronlike, berylliumlike, and lithiumlike krypton; for the 800 MeV ion beam the transitions belonged primarily to berylliumlike and lithiumlike krypton. Partial Grotrian diagrams for the berylliumlike and lithiumlike cases are shown in Fig. 1. All wavelength analysis was done on spectra obtained with the 610 MeV ion beam, because this yielded the highest ion beam intensities and was available for most of the accelerator time. The transitions present in the spectra were identified as $n = 2-2$ transitions and high- n Rydberg transitions in the first, second, and third orders of diffraction. A typical spectrum, recorded in a single exposure of the PSD, is displayed in Fig. 2.

Table 1. Wavelengths of the Rydberg transition structures calculated using different population models.

Transition	$2J + 1$ (Å)	L^2 (Å)	Diff. (Å)
Li-like $n = 6-7$	106.790	106.802	0.012
Li-like $n = 7-8$	164.591	164.610	0.019

Table 2. Wavelengths of the Rydberg transition structures calculated for different beam lengths viewed.

Transition	0–100 μm	0–150 μm	25–125 μm	50–150 μm	50–200 μm
Li-like $n = 6-7$	106.790 Å	106.796 Å	106.810 Å	106.818 Å	106.820 Å
Li-like $n = 7-8$	164.591 Å	164.600 Å	164.612 Å	164.623 Å	164.628 Å

Over 30 such overlapping spectra covered the 50–300 Å wavelength region. The wavelength dispersion was determined from lithiumlike ion Rydberg transitions as in-beam reference lines. These transitions can be accurately modeled (see refs. 3 and 5–12). The use of such largely unresolved Rydberg spectral features as wavelength references requires a calculation of the wavelengths, intensities and decays of the fine-structure components.

The lithiumlike krypton $n = 6-7$ and $n = 7-8$ Rydberg transitions near 107 and 165 Å in first order, respectively, and the same $n = 6-7$ Rydberg transition appearing in second order near 214 Å were used for the wavelength calibration. Following a procedure given elsewhere [3], the reference wavelengths were calculated to be 106.790 Å for the $n = 6-7$ transition and 164.591 Å for the $n = 7-8$ Rydberg transition. As similar analyses of Rydberg transition structures of this type have shown, the dominant uncertainty to the reference wavelengths resides in the position of the target foil and in the assumed fine-structure-line intensity pattern, which depends on the only approximately known excited state population distribution from the beam-foil interaction. Table 1 lists the effect of the choice of population distribution on the calculated reference wavelengths. The $2J + 1$ population model was chosen for the reference values; the differences, 0.012 and 0.019 Å, respectively, from a calculation based on an L^2 population model was taken to represent the uncertainty of the procedure. Table 2 gives the effect of the foil position on the final reference wavelengths in terms of different beam lengths viewed. The beam length viewed is defined by the entrance slit width and the $\sim f/50$ geometry of the spectrometer. Since the entrance slit was positioned close to the ion beam, the width of the slit, 100 μm , was effectively the length of beam observed. The values in Table 2, for different beam lengths viewed, assume a conservative uncertainty in foil position of 50 μm in either the upstream or the downstream portion. The largest difference among these values, 0.030 and 0.037 Å, was used to establish the uncertainty in the final reference wavelength values. Other factors that affect the uncertainty of the reference wavelength values have more than an order of magnitude smaller effects than the two discussed above. These other effects include the polarization model of the electron structure, uncertainties of excited state lifetimes and transition probabilities, influences of cascade repopulation, ion-beam energy, and line shape fitting [3]. Summing the two dominant contributions to the uncertainties in quadrature leads to reference wavelength values of 106.790(32) and 164.591(42) Å for the lithiumlike krypton ion $n = 6 - 7$ and $n = 7 - 8$ Rydberg transitions, respectively.

To establish the wavelength dispersion, the reference wavelengths with their centroid locations, relative to the detector position established by the grating equation from over 20 observed spectra, were fit to a polynomial function. By concentrating the analysis on only a $\sim 40\%$ section of the detector in which line shapes were symmetric and narrow, more reliable and consistent results for the wavelength dispersion function were achieved.

Table 3. Lithiumlike krypton $n = 2-2$ transition wavelengths.

Transition	Experiment		Theory	
	λ (Å)	Ref.	λ (Å)	Ref.
$1s^2 2s^2 S_{1/2} - 1s^2 2p^2 P_{3/2}$	91.02(6)		90.97	18
	91.08(10)	13	91.051	19
	91.06(2)	14	91.049	20
	91.049(25)	15	91.034	21
	91.00(3)	16		
$1s^2 2s^2 S_{1/2} - 1s^2 2p^2 P_{1/2}$	90.99(8)	17		
	174.05(8)		173.5	18
	174.15(26)	13	174.04	19
	174.03(3)	14	174.04	20
	174.036(26)	15	173.98	21
	173.93(4)	16		

Table 4. Berylliumlike krypton $n = 2-2$ transition wavelengths.

Transition	Experiment		Theory	
	λ (Å)	Ref.	λ (Å)	Ref.
$2s^2 \ ^1S_0 - 2s2p \ ^1P_1$	72.62(5)		72.27	18
	72.78(2)	14	72.761	22
	72.756(20)	15		
	72.66(5)	16		
$2s2p \ ^3P_2 - 2p^2 \ ^1D_2$	72.62(5)		72.19	18
	72.66(5)	16	72.518	22
$2s2p \ ^3P_1 - 2p^2 \ ^3P_2$	75.62(5)		75.47	18
	75.66(5)	16	75.761	22
$2s2p \ ^3P_0 - 2p^2 \ ^3P_1$	75.62(5)		75.50	18
	75.66(5)	16	75.617	22
$2s2p \ ^1P_1 - 2p^2 \ ^1S_0$	76.97(7)		77.11	18
	77.10(5)	16	77.101	22
$2s2p \ ^3P_1 - 2p^2 \ ^3P_1$	80.50(7)		80.67	18
	80.75(8)	16	80.715	22
$2s2p \ ^1P_1 - 2p^2 \ ^1D_2$	98.20(8)		98.70	18
	98.19(10)	16	98.235	22
$2s2p \ ^3P_2 - 2p^2 \ ^3P_2$	111.73(5)		110.8	18
	111.65(5)	16	111.711	22
$2s2p \ ^3P_1 - 2p^2 \ ^3P_0$	117.73(5)		117.2	18
	117.74(10)	16	117.646	22
$2s2p \ ^3P_2 - 2p^2 \ ^3P_1$	122.83(6)		122.4	18
	123.10(20)	16	122.828	22
$2s^2 \ ^1S_0 - 2s2p \ ^3P_1$	169.81(10)		169.8	18
	169.9(5)	13	169.899	22
	169.850(25)	14		
	169.845(25)	15		
$2s2p \ ^3P_1 - 2s2p \ ^3P_2$	170.03(20)	16		
	235.48(5)	15	236.5	18
			235.417	22

Table 5. Boronlike krypton $n = 2-2$ transition wavelengths.

Transition	Experiment		Theory	
	λ (Å)	Ref.	λ (Å)	Ref.
$2s^2 2p^2 P_{3/2} - 2s 2p^2 P_{3/2}$	64.65(10)	15	64.32	18
	64.59(20)	16		
	64.651(10)	23		
$2s^2 2p^2 P_{3/2} - 2s 2p^2 P_{1/2}$	64.65(10)	15	64.96	18
	65.00(20)	16		
	65.067(25)	23		
$2s^2 2p^2 P_{1/2} - 2s 2p^2 S_{1/2}$	66.49(5)	16	66.30	18
$1s^2 2s^2 2p^2 P_{1/2} - 2s 2p^2 D_{3/2}$	69.957(20)	15	69.82	18
	69.84(5)	16		
$2s 2p^2 P_{3/2} - 2p^3 P_{3/2}$	78.90(20)	16	78.86	18
$2s 2p^2 D_{3/2} - 2p^3 D_{3/2}$	82.96(25)		83.10	18
$2s^2 2p^2 P_{3/2} - 2s 2p^2 D_{5/2}$	84.67(19)		84.93	18
	84.94(10)	15		
	84.89(5)	16		
	84.454(25)	23		
$2s 2p^2 S_{1/2} - 2p^3 D_{3/2}$	88.23(25)		88.71	18
$2s 2p^2 D_{5/2} - 2p^3 D_{5/2}$	94.11(25)		93.48	18
	93.75(20)	16		
$2s^2 2p^2 P_{1/2} - 2s 2p^2 P_{1/2}$	143.266(10)	23	144.9	18
$2s^2 2p^2 P_{3/2} - 2s 2p^2 P_{5/2}$	151.121(25)	23	152.3	18
$2s^2 2p^2 P_{1/2} - 2s^2 2p^2 P_{3/2}$	203.021(20)	15	203.7	18

For the lithiumlike and berylliumlike ion transitions, line blending from boronlike and carbonlike ion $n = 2-2$ and Rydberg transitions was possible. Therefore, nearly all the transitions were observed in first, second, and in some instances third order of diffraction, which helped to distinguish and eliminate some cases of line blending. Tables 3–5 present our measured wavelengths for lithiumlike, berylliumlike, and boronlike ion $n = 2-2$ transitions. Tables 3–5 include previous measurements and theoretical calculations [13–23] of the $n = 2-2$ transitions in these few-electron krypton ions. Graphical comparisons of these measurements and calculations are shown in Fig. 3.

The $2s^2 S_{1/2} - 2p^2 P_{1/2}$ resonance transition of the lithiumlike krypton ion has a wavelength near 174 Å. This line unfortunately is blended with the $n = 7-8$ Rydberg transition feature of berylliumlike krypton, located near 175 Å. The complex Rydberg structure of the berylliumlike ion precludes any multi-Gaussian line-shape fitting [24–27], necessitating alternate means for determining the lithiumlike wavelength. While the $2^2 P_{1/2}$ excited level of the Li-like ion has a lifetime of 360 ps, the berylliumlike ion $n = 8$ Rydberg state has a lifetime of <3 ps. Consequently, the recording of sufficiently time-delayed spectra removes the blending caused by the Rydberg transition. The long-lived (2.5 ns) berylliumlike ion $2s^2 ^1S_0 - 2s 2p^3 P_1$ intercombination transition near 170 Å was blended with the shorter lived (70 ps) boronlike $2s^2 2p^2 P_{3/2} - 2s 2p^2 D_{5/2}$ transition in second order at 85×2 Å, and this blend was also disentangled by recording delayed spectra.

There are two unresolved blends among the berylliumlike krypton ion $n = 2-2$ transitions. The first of these involves the $2s^2 ^1S_0 - 2s 2p^3 P_1$ resonance transition blended with the $2s 2p^3 P_2 - 2p^2 ^1D_2$ transition near 73 Å, and the second of these involves the $2s 2p^3 P_1 - 2p^2 ^3P_2$ transition blended with the $2s 2p^3 P_0 - 2p^2 ^3P_1$ transition near 76 Å. The wavelength values quoted in Table 4 for these transitions represent the result of fitting the blended profile to a single Gaussian and extracting a single wavelength value from the centroid. This procedure is similar to that used by Martin et al. [16] for this line blending.

Fig. 3. Comparisons between measured and calculated wavelengths for $n = 2-2$ transitions in lithiumlike and berylliumlike krypton ions. The squares and their error bars represent measurements and the triangles represent theoretical calculations. Source references are: Dietrich et al. [13], Denne and co-workers [14, 15], Martin et al. [16], Büttner et al. [17], Cheng et al. [18], Kim et al. [19], Theodosiou et al. [20], Johnson et al. [21], and Safronova et al. [22].

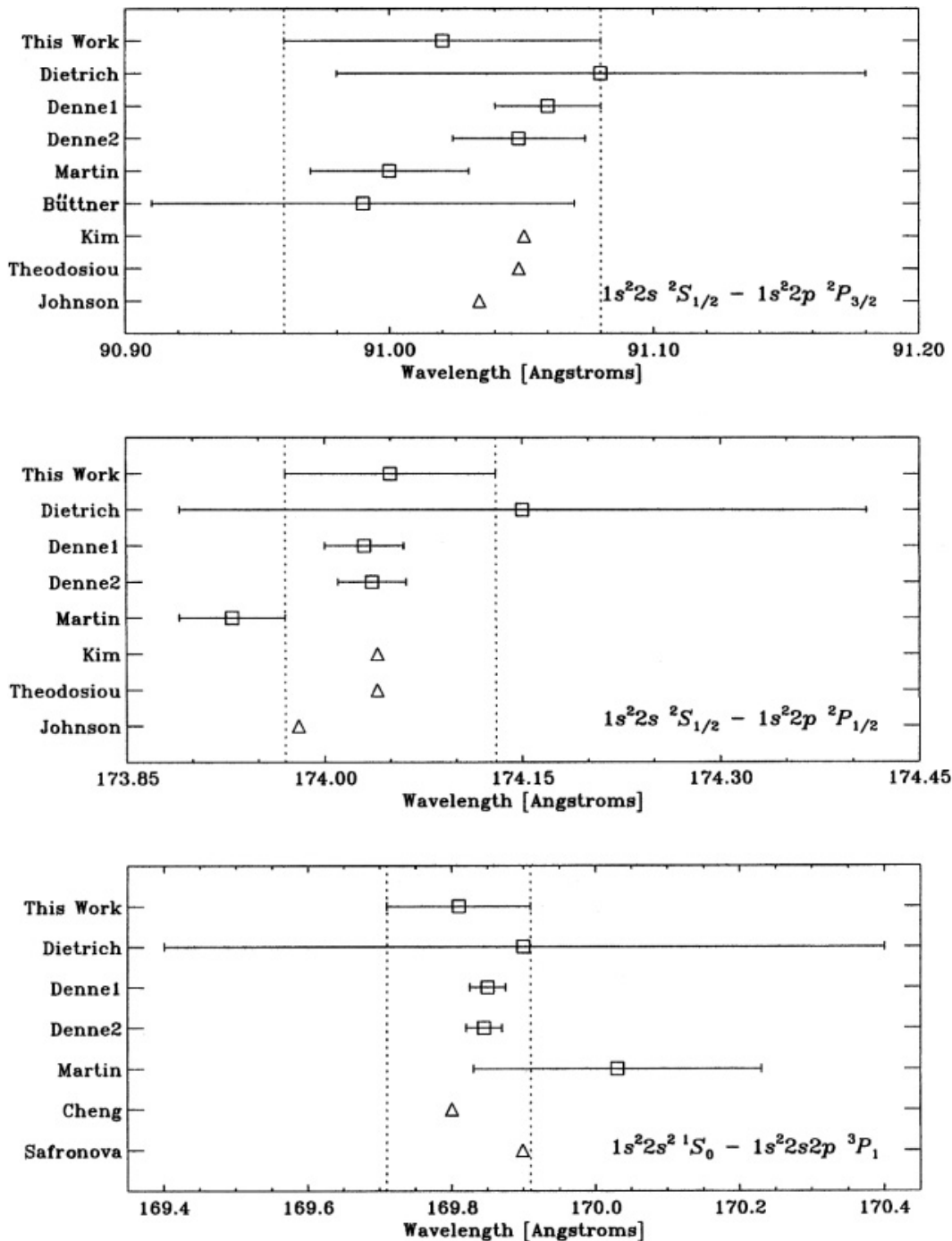
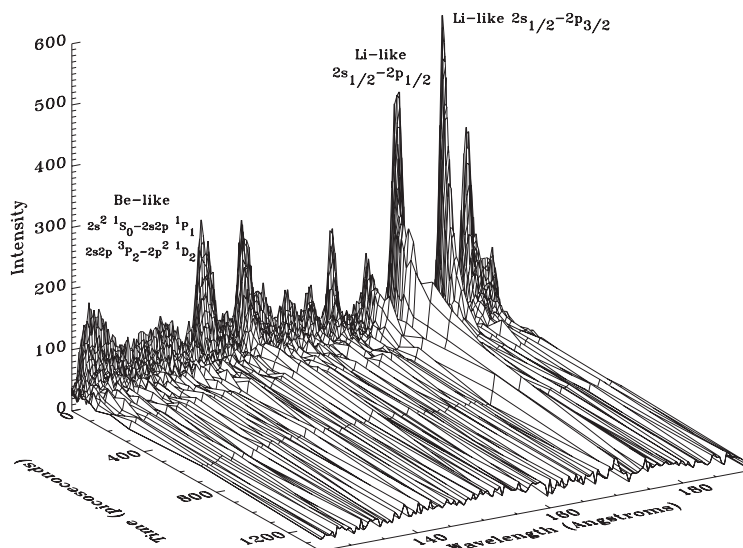


Fig. 4. Spectra of highly ionized krypton recorded for a sequence of positions along the ion beam, representing time delays of up to 1.2 ns following excitation.

Sequence of Time-Delayed Krypton Spectra



The removal of the blending through observations of time-delayed spectra will not work in this case, because the upper states of each of the transitions have similar predicted lifetimes (~ 10 ps).

4. Lifetimes

Exploiting the fact that distance from the foil along the ion beam relates to time after excitation, the individual spectra recorded at different distances (achieved by displacing the exciter foil) represent time-resolved delayed spectra, from which decay curves of individual spectral features can be constructed. Twenty or more individual spectra each at a different foil position were recorded while the PSD was held fixed at a particular wavelength position. A typical landscape plot of the spectra for one foil position is shown in Fig. 4. With the 610-MeV krypton ion beam, 9 such lifetime scans were recorded, each covering a different wavelength region. With the 800 MeV krypton ion beam, 14 lifetime scans were recorded. As the lifetimes of interest ranged from 10 ps to 2.5 ns, the pattern of distances, or equivalently the time intervals, between the foil positions was optimized for the measurements of short or long decays. The individual spectra were normalized to the charge collected in the Faraday cup.

Decay curves were produced from the accumulated signal in each spectrum, summing the number of counts in a narrowly defined region containing a peak which represented a $n = 2-2$ transition in lithiumlike or berylliumlike krypton ions. As with the wavelength analysis, possible line blending was eliminated by measuring the decays in several orders of diffraction. For the case of the berylliumlike ion $2p^2$ excited levels, lifetimes were measured by observing alternate branches from the given excited levels, which helped eliminate some cases of blending. Further consistency checks were made in the lifetime analysis by summing the number of counts for a particular transition over different channel regions.

The decay curves were analyzed by fits of a single exponential function plus a constant background term to the data. The velocity of the ion beam was determined from the ATLAS accelerator ion beam energy setting and corrected for energy loss within the target foil. For the 610 MeV krypton ion beam a

Table 6. Highly ionized krypton $n = 2$ state lifetimes.

State	Experiment		Theory	
	τ (ps)	Ref.	τ (ps)	Ref.
$2p^2P_{1/2}$	365(23)		356.0	18
	320(30)	13	357.5	20
			359.8	21
$2p^2P_{3/2}$	50.7(9)		49.70	18
	52(3)	13	49.64	20
	49.5(1.5)	29	49.93	21
$2s2p^3P_1$	2560(240)		2480	18
	2300(300)	13	2420	30
$2s2p^1P_1$	17.5(1.5)	29	17.2	18
			18.5	30
$2p^2^3P_0$	47.4(4.7)		48.0	18
$2p^2^3P_1$	21.0(1.7)		22.7	18
$2p^2^3P_2$	29.1(2.6)		30.8	18
$2p^2^1D_2$	19.9(1.2)		18.6	18
	19(2)	29		
$2p^2^1S_0$	10.6(1.0)		10.0	18
	10.5(1.0)	29		

217 $\mu\text{g}/\text{cm}^2$ carbon foil was used, which resulted in an energy loss of 8.2 MeV. For the 800 MeV krypton ion beam a 50 $\mu\text{g}/\text{cm}^2$ carbon foil was used, which resulted in an energy loss of 1.7 MeV [28]. Our lifetime results are compared with previous measurements [13, 29] and with calculations [18, 20, 21, 30] in Table 6 and Fig. 5. It should be noted that much of the data presented here were preliminarily reported earlier [31], in the same time frame as ref. 29.

The interaction of fast ions with the exciter foils is nonselective, and the appearance of high- n Rydberg decays (more precisely, of high- n, l yrast transitions) indicates that levels much higher than $n = 2$ are populated in the process. These levels repopulate the lower lying levels that are of our primary interest. In principle, such repopulation can be taken into account by measuring the time dependence of the direct cascades into the level of interest [32], and then the correct decay probability of the level of interest extracted from a correlated analysis. In the present case, the direct cascades fall into the EUV and X-ray bands that we do not observe, and the directly feeding levels have predicted lifetimes of the order of 10 fs [33], much too short for achieving appropriate time resolution in the experiment. The levels of interest in the Li-like Kr ion, for example, $2^2P_{1/2}$ and $2^2P_{3/2}$, have lifetimes of about 360 and 50 ps, respectively. This is very much longer than the typical cascades (and even many of their repopulating cascades). Consequently, one may assume that the fast cascades boost the population of the $n = 2$ levels, but do not noticeably distort the decay curves on a time scale that would affect the analysis. All our present evaluations make this assumption.

An alternate approach is the modeling of the population (as was done for the time-dependent reference lines) of the Rydberg levels, and investigating the effect of the cascades on simulated decay curve data, because the yrast cascade chain is known to cause long tails of affected decay curves. Such an approach has been tried for Li-like Kr ions elsewhere [29], and a slight, but significant effect was seen on the fitted lifetime value.

For the $\text{Kr}^{33+} 2p^2P_{3/2}$ lifetime, our measured value agrees with the values of previous, less precise measurements (see Table 6). For the $\text{Kr}^{33+} 2p^2P_{1/2}$ lifetime, our result also overlaps with the previous measurement, but shows better agreement with theoretical calculations.

Fig. 5. Comparisons between measured and calculated lifetimes for $n = 2$ states in lithiumlike and berylliumlike krypton ions. The squares and their error bars represent measurements and the triangles represent theoretical calculations. Source references are: Dietrich et al. [13], Träbert et al. [29], Cheng et al. [18], Theodosiou et al. [20], Johnson et al. [21], and Curtis and Ellis [30].

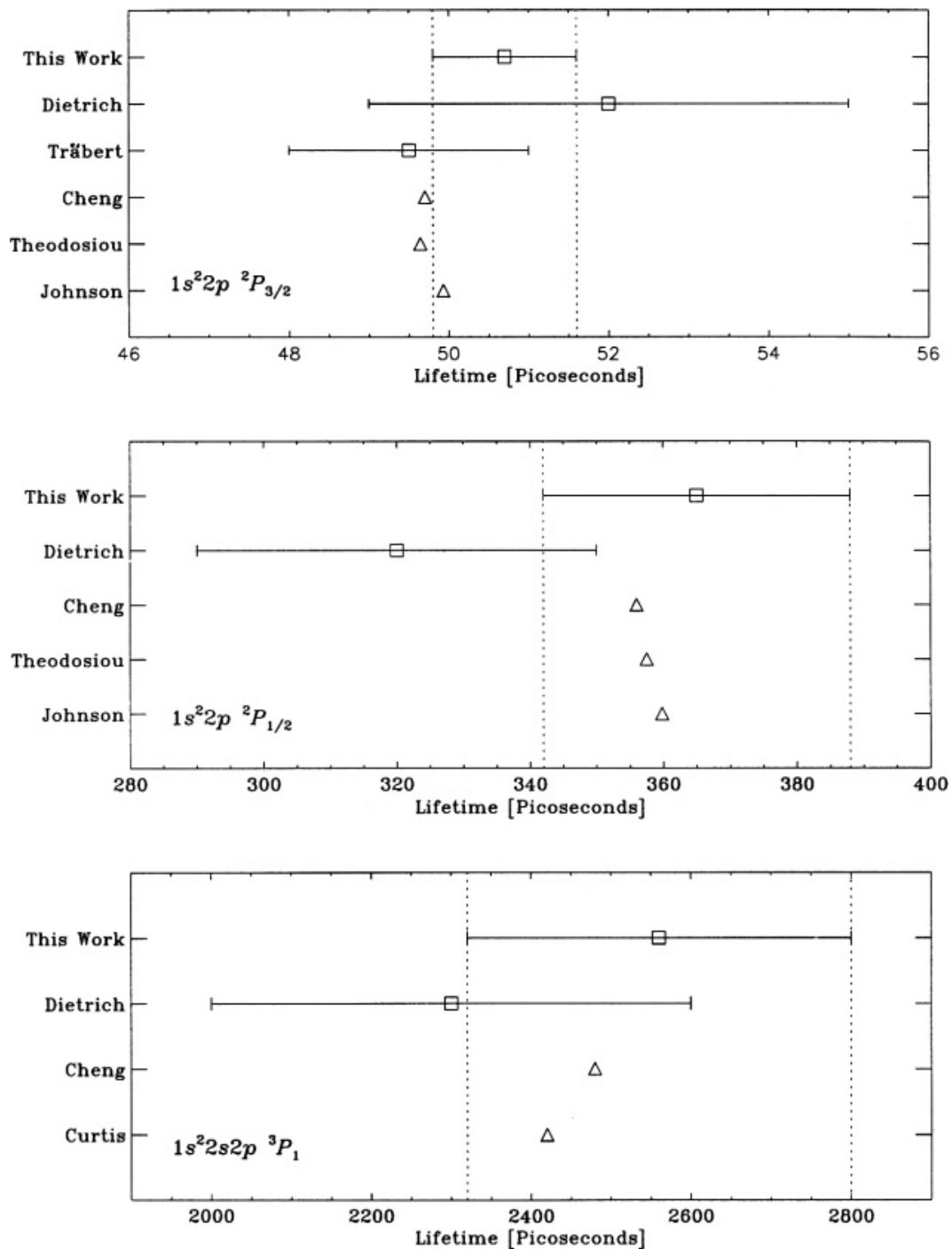


Fig. 6. Isoelectronic plot of charge-scaled, relativistically corrected line strengths for the Li sequence. Symbols update the experimental measurements compiled in ref. 34. The continuous lines trace the theoretical calculations of ref. 21. The ordinate has been relativistically corrected by renormalizing to the Dirac hydrogenic line strength.

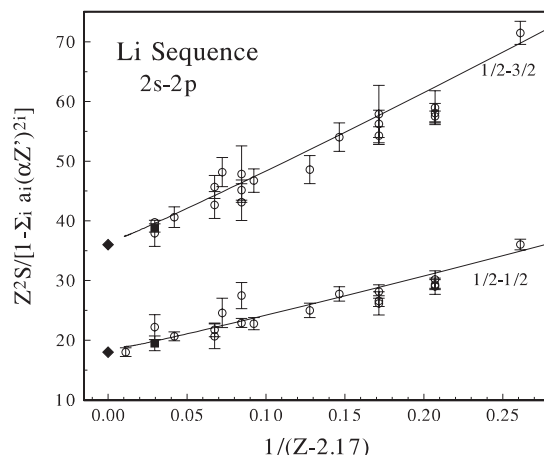


Fig. 7. Isoelectronic plot for charge-scaled, intermediate-coupling-corrected reduced line strengths for the Be sequence. Symbols update the experimental measurements compiled in ref. 30. The continuous and broken lines trace the theoretical calculations of ref. 35.

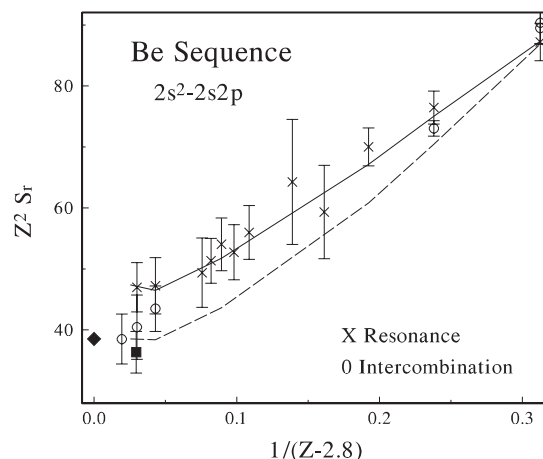


Figure 6 displays a plot of the charge-scaled line strength versus the reciprocal screened charge for the Li isoelectronic sequence. The screening parameter 2.17 was chosen to optimize the linearity of the plot. Li I, Be II, and B III were omitted to better reveal the high- Z behaviour. Here, the ordinate has been relativistically corrected by renormalizing to the Dirac value for the hydrogenic line strength, as recommended in ref. 34. Open circles denote the experimental values cited earlier in ref. 34, and solid squares denote the measurements reported herein. The solid diamonds denote the nonrelativistic hydrogenic value, which the trend of the data confirms to be the high- Z limit. Error bars indicate the quoted uncertainties. The continuous lines trace theoretical calculations [21].

Figure 7 displays a plot of the charge-scaled intermediate-coupling-reduced strength versus the reciprocal screened charge for the Be isoelectronic sequence. The screening parameter 2.8 was chosen to optimize the linearity of the plot. Be I and B II were here again omitted to better reveal the high- Z behaviour. The reduction of intermediate coupling effects was accomplished by computing the singlet-

triplet mixing amplitudes from the energy level data, and using these to correct the resonance and intercombination line strengths, as described in ref. 30. Open circles denote the experimental values cited earlier in ref. 30, and the solid square denotes the measurement reported herein. The solid diamond again denotes the nonrelativistic hydrogenic value, and error bars indicate the quoted uncertainties. The continuous and broken lines trace theoretical calculations [35].

Acknowledgments

We are grateful to the ATLAS staff for expert technical assistance during this experiment. This work was undertaken under support from the US DOE Office of Basic Energy Sciences under Contract Nos. W-31-109-ENG-38 (ANL), DE-FG02-92ER14283 (Notre Dame), and DE-FG02-94ER14461 (University of Toledo). We thank E. Träbert (Bochum and Livermore) for valuable advice.

References

1. L. Barrette. *Phys. Scr.* **10**, 213 (1974).
2. H.G. Berry, J. Desesquelles, P. Tryon, P. Schnur, and G. Gabrielse. *Phys. Rev. A*, **14**, 1457 (1976).
3. K.W. Kukla, A.E. Livingston, J. Suleiman, H.G. Berry, R.W. Dunford, D.S. Gemmell, E.P. Kanter, S. Cheng, and L.J. Curtis. *Phys. Rev. A*, **51**, 1905 (1995).
4. Y. Baudinet-Robinet. *Nucl. Instrum. Methods*, **190**, 197 (1981).
5. W.A. Davis and R. Marrus. *Phys. Rev. A*, **15**, 1963 (1977).
6. H.G. Berry, R. DeSerio, and A.E. Livingston. *Phys. Rev. Lett.* **41**, 1652 (1978).
7. R. O'Brien, J.D. Silver, N.A. Jelley, S. Bashkin, E. Träbert, and P.H. Heckmann. *J. Phys. B*, **12**, L41 (1979).
8. R. DeSerio, H.G. Berry, R.L. Brooks, J. Hardis, A.E. Livingston, and S.J. Hinterlong. *Phys. Rev. A*, **24**, 1872 (1981).
9. H.A. Klein, F. Moscatelli, E.G. Myers, E.H. Pinnington, J.D. Silver, and E. Träbert. *J. Phys. B*, **18**, 1483 (1985).
10. E.J. Galvez, A.E. Livingston, A.J. Mazure, H.G. Berry, L. Engström, J.E. Hardis, L.P. Somerville, and D. Zei. *Phys. Rev. A*, **33**, 3667 (1986).
11. R. Büttner, B. Kraus, M. Nicolai, K.-H. Schartner, F. Folkmann, P.H. Mokler, and G. Möller. *Z. Phys. D*, **22**, 693 (1992).
12. D.J.H. Howie, J.D. Silver, and E.G. Myers. *Phys. Rev. A*, **52**, 1761 (1995).
13. D.D. Dietrich, J.A. Leavitt, H. Gould, and R. Marrus. *Phys. Rev. A*, **22**, 1109 (1980); *J. Phys. (Paris)*, **40**, C1-215 (1979).
14. B. Denne and E. Hinnov. *Phys. Scr.* **35**, 811 (1987).
15. B. Denne, E. Hinnov, J. Ramette, and B. Saoutic. *Phys. Rev. A*, **40**, 1488 (1989); E. Hinnov and B. Denne. *Phys. Rev. A*, **40**, 4357 (1989); B. Denne-Hinnov. *Phys. Rev. A*, **45**, 2135 (1992).
16. S. Martin, A. Denis, M.C. Buchet-Poulizac, J.P. Buchet, and J. Désesquelles. *Phys. Rev. A*, **42**, 6570 (1990).
17. R. Büttner, B. Kraus, M. Nicolai, K.-H. Schartner, F. Folkmann, P.H. Mokler, and G. Möller. *AIP Conf. Proc.* **274**, 423 (1993).
18. K.T. Cheng, Y.-K. Kim, and J.P. Desclaux. *At. Data Nucl. Data Tables*, **24**, 111 (1979).
19. Y.-K. Kim, D.H. Baik, P. Indelicato, and J.P. Desclaux. *Phys. Rev. A*, **44**, 148 (1991).
20. C.E. Theodosiou, L.J. Curtis, and M. El-Mekki. *Phys. Rev. A*, **44**, 7144 (1991).
21. W.R. Johnson, Z.W. Liu, and J. Sapirstein. *At. Data Nucl. Data Tables*, **64**, 279 (1996).
22. M.S. Safronova, W.R. Johnson, and U.I. Safronova. *Phys. Rev. A*, **53**, 4036 (1996).
23. R. Myrnäs, C. Jupén, G. Miecznik, I. Martinson, and B. Denne-Hinnov. *Phys. Scr.* **49**, 429 (1994).
24. A.J. Mazure, A.E. Livingston, E.J. Galvez, and S.J. Hinterlong. *Phys. Rev. A*, **32**, 3775 (1985).
25. R. König, K.-H. Kolk, K.N. Koshelev, and H.-J. Kunze. *Phys. Rev. Lett.* **62**, 1750 (1989).
26. A.E. Livingston, E.J. Galvez, and F.G. Serpa. *Phys. Rev. Lett.* **64**, 2335 (1990).
27. F.G. Serpa and A.E. Livingston. *Phys. Rev. A*, **43**, 6447 (1991).
28. J.F. Ziegler. *Handbook of stopping cross sections for energetic ions in all elements*. Pergamon Press, New York. 1980.

29. E. Träbert, J. Doerfert, J. Granzow, R. Büttner, J. Brauckhoff, M. Nicolai, K.-H. Schartner, F. Folkmann, and P.H. Mokler. *Phys. Lett.* **202A**, 91 (1995).
30. L.J. Curtis and D.G. Ellis. *J. Phys. B*, **29**, 645 (1996).
31. E. Jasper, A. Vasilyev, K. Kukla, C. Vogel Vogt, H.G. Berry, S. Cheng, L.J. Curtis, and R. Dunford. *Phys. Scr. T*, **80**, 466 (1999).
32. L.J. Curtis, H.G. Berry, and J. Bromander. *Phys. Lett.* **34**, 169 (1971).
33. H.L. Zhang, D.H. Sampson, and C.J. Fontes. *At. Data Nucl. Data Tables*, **44**, 31 (1990).
34. L.J. Curtis, D.G. Ellis, and I. Martinson. *Phys. Rev. A*, **51**, 251 (1995).
35. A. Ynnerman and C. Froese Fischer. *Phys. Rev. A*, **51**, 2020 (1995).